

Efficient Transmitter Selection Strategies for Improved Information Gathering of Aerial Vehicle Navigation in GNSS-Denied Environments

Alexander A. Nguyen , University of California, Irvine, CA 92697 USA
Zaher M. Kassas , The Ohio State University, Columbus, OH 43210 USA

INTRODUCTION

Modern aerial vehicle navigation systems, whether low-altitude unmanned aerial vehicles (UAVs) or high-altitude aircraft, rely on global navigation satellite system (GNSS) signals [1]. However, relying on GNSS alone does not yield a continuous flow of resilient position, velocity, and time estimates. In recent years, GNSS radio frequency interference (RFI) incidents have increased dramatically, threatening the safety of flight operations [2], calling for a reliable alternative to GNSS signals in the event that these signals become unusable [3]. Signals of opportunity (SOPs) [4], [5], [6], [7] have been the subject of extensive research, where they have shown promise to be a stand-alone navigation alternative to GNSS. SOPs can be terrestrial-based (e.g., FM radio [8], [9], cellular [10], [11], [12], [13], and digital television [14], [15]) or space-based (e.g., low Earth orbit (LEO) satellites [16], [17], [18]). Among terrestrial SOPs, cellular signals have shown the most promise for aerial vehicle navigation [19], achieving submeter-level accuracy in a standalone [20] and differential [21] navigation fashion.

Assessing terrestrial SOPs on low-altitude UAVs and high-altitude aircraft has been considered in the context of channel modeling, communication, and navigation [22], [23], [24], [25]. Of particular note is the recent week-long flight campaign by the Autonomous Systems Perception, Intelligence, and Navigation (ASPIN) Laboratory in collaboration with the U.S. Air Force (USAF) to study the potential of

cellular SOPs for high-altitude aircraft navigation. This campaign, called “SNIFFER: Signals of opportunity for Navigation In Frequency-Forbidden EnviRonments,” revealed that terrestrial cellular SOPs can be acquired and tracked at altitudes reaching 23,000 ft above ground level and at horizontal distances of more than 100 km away, and could yield meter-level accurate navigation solutions without GNSS [26], [27].

At high altitudes, it was recently discovered that more than a hundred cellular SOPs can be acquired and tracked, from which pseudorange measurements can be extracted [28]. Tracking all such SOPs simultaneously could be formidable on platforms with limited size, weight, power, and cost (SWaP-C) or unnecessary, since tracking a subset of the SOPs could yield a comparable performance. As such this article considers the transmitter selection problem, where an aerial vehicle is tasked with selecting a subset of the SOPs, to minimize the receiver’s computational strain. Figure 1 illustrates a real-world scenario in which the problem of transmitter selection was encountered. Here, the white pins denote $M = 57$ cellular SOPs which the aerial vehicle-mounted receiver was able to acquire and track.

A similar problem to transmitter selection has been studied in the literature in the context of sensor selection for target tracking [29], [30]. Sensor selection problems are typically formulated as an integer programming (IP) problem, which is difficult to solve in a computationally efficient fashion, while finding the optimal solution via exhaustive search becomes formidable for large sensor networks. To circumvent this, several heuristic and suboptimal algorithms have been proposed. Some approaches formulate the sensor selection problem as a convex or nonconvex optimization problem [31], [32], [33], [34], [35]. Others have approached this problem as a greedy sensor selection by leveraging the notion of submodularity [36], [37] or by utilizing the Fisher information matrix (FIM) [38], [39].

It is rather difficult to explicitly solve the transmitter selection optimization problem efficiently for a large number of transmitters due to the integer constraints. As such, this article aims to extend the findings in [40] by proposing two

Authors’ current address: Alexander A. Nguyen is with the University of California, Irvine, CA 92697 USA (e-mail: alexaan2@uci.edu). Zaher M. Kassas is with The Ohio State University, Columbus, OH 43210 USA (e-mail: zkassas@ieee.org).

Manuscript received 11 November 2022; accepted 6 April 2023, and ready for publication 12 April 2023.

Review handled by Daniel O’Hagan.

0885-8985/23/\$26.00 © 2023 IEEE



Image licensed by Ingram Publishing

suboptimal, computationally efficient transmitter selection strategies, termed opportunistic greedy selection (OGS) and one-shot selection (OSS). The proposed strategies are simple, yet highly effective at selecting the “best” transmitters without explicitly solving the IP problem. The proposed strategies exploit the additive, iterative properties of the FIM, where the OGS selects the most informative transmitters in finite iterations (i.e., recursively), while the OSS selects in one iteration (i.e., batch). Numerical simulations are presented analyzing the performance of the proposed selection strategies, where it is concluded that OGS performs closely to the optimal selection, while executing in a fraction of the optimal selection’s time. Experimental results are also presented for a USAF high-altitude aircraft navigating without GNSS in a rural and a semiurban region. The effectiveness of the selected SOPs on the navigation performance is also demonstrated. The position

root-mean-squared error (RMSE) with the optimal, OGS, and OSS were 4.53, 6.28, and 7.13 m in the rural region; and 5.83, 6.08, and 6.70 m in the semiurban region for an aircraft traversing a trajectory of 1.48 and 1.22 km, respectively. It is important to highlight that the SOP selection subset was found to be valid over a trajectory of several kilometers, since the aerial vehicle-to-SOP geometry is approximately stationary for sufficiently faraway SOPs.

The rest of this article is organized as follows. The “Problem Description” section overviews the considered problem. The “Problem Formulation” section formulates the transmitter selection problem. The “Transmitter Selection Framework” section presents the selection strategies. The “Selection Strategy Analysis” section analyzes the proposed selection strategies. We then present the “Simulation Results,” section. The “Experimental Results” section provides

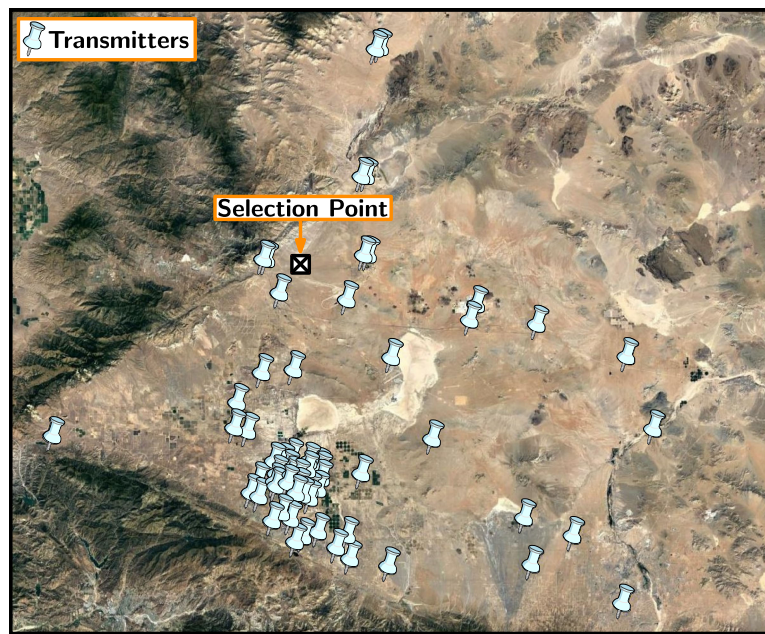


Figure 1.

Motivating example. $M = 57$ terrestrial SOP transmitters (white) in the environment relative to the aerial vehicle’s selection point (black cross). What is the “best” (most informative) $K < M$ subset of SOPs for navigation?

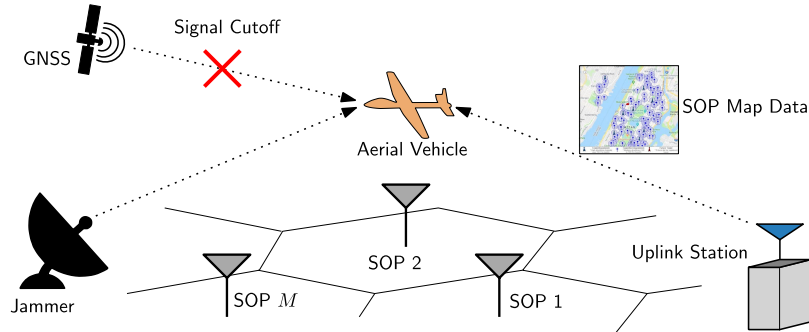


Figure 2.

Problem description. An aerial vehicle is equipped with a receiver capable of extracting pseudorange measurements from terrestrial SOPs. During flight, the aerial vehicle experiences GNSS outage. A nearby uplink station sends SOP map data to the aerial vehicle, which contains the locations of M terrestrial SOPs. The aerial vehicle's selects the “best” (most informative) $K < M$ to use to continue navigating.

experimental results for an aerial vehicle flying in two different regions. Finally, we present the “Conclusions” section.

PROBLEM DESCRIPTION

To motivate the transmitter selection problem, consider the scenario depicted in Figure 2, in which an aerial vehicle is navigating in an environment comprising M terrestrial SOP transmitters. During flight, the aerial vehicle experiences GNSS outage (e.g., due to RFI or spoofing). The aerial vehicle is assumed to have a map of the SOP locations (e.g., loaded prior to flight or transmitted from a nearby uplink station). The aerial vehicle is assumed to be equipped with receivers capable of extracting pseudorange measurements from the SOPs, which will be used instead of GNSS to navigate the aerial vehicle. Due to SWaP-C constraints (e.g., limited payload, processing power, etc.), the aerial vehicle can only use signals from ($K < M$) SOPs. What is the “best” (most informative) SOP subset to select?

PROBLEM FORMULATION

This section formulates the transmitter selection problem.

PSEUDORANGE MEASUREMENT MODEL

Consider an aerial vehicle equipped with an onboard receiver capable of extracting pseudorange measurements from M terrestrial SOPs in the environment. The pseudorange measurement made by the receiver to the i th SOP, after discretization and mild approximations, is modeled as

$$z_{s_i}(k) = \underbrace{\|\mathbf{r}_r(k) - \mathbf{r}_{s_i}\|_2 + c \cdot [\delta t_r(k) - \delta t_{s_i}(k)]}_{h_i(\mathbf{x}(k))} + v_{s_i}(k) \quad (1)$$

where, $\mathbf{r}_r = [x_r, y_r, z_r]^\top$ is the three-dimensional (3D) position vector of the aerial vehicle, $\mathbf{r}_{s_i} = [x_{s_i}, y_{s_i}, z_{s_i}]^\top$

is the 3D position vector of the i th SOP, δt_r is the aerial vehicle-mounted receiver’s clock bias, δt_{s_i} is the i th SOP’s clock bias, c is the speed of light, and v_{s_i} is the i th SOP’s measurement noise, which is modeled as a zero-mean white Gaussian sequence with variance $\sigma_{s_i}^2$ and is assumed to be independent across all SOPs. The dynamics of the clock error is described in Appendix A.

FISHER INFORMATION MATRIX

The proposed transmitter selection strategies aim to choose the most informative measurements, which motivates adopting the FIM defined as

$$\mathbf{I}(\mathbf{x}) = \mathbb{E} \left[\left(\frac{\partial \ln p(\mathbf{z}|\mathbf{x})}{\partial \mathbf{x}} \right) \left(\frac{\partial \ln p(\mathbf{z}|\mathbf{x})}{\partial \mathbf{x}} \right)^\top \right]$$

where, $p(\mathbf{z}|\mathbf{x})$ is the likelihood function of the measurements \mathbf{z} parameterized by the states \mathbf{x} . Since the noise in the measurement model (1) is assumed to be independent across all SOPs, the FIM can be written as the prior FIM plus a summation of the information content associated with each measurement, that is,

$$\begin{aligned} \mathbf{I}(\mathbf{x}) &= \mathbf{I}_0(\mathbf{x}) + \sum_{i=1}^M \frac{1}{\sigma_{s_i}^2} \left(\frac{\partial h_i(\mathbf{x})}{\partial \mathbf{x}} \right) \left(\frac{\partial h_i(\mathbf{x})}{\partial \mathbf{x}} \right)^\top \\ &= \mathbf{I}_0(\mathbf{x}) + \sum_{i=1}^M \mathbf{I}_i(\mathbf{x}). \end{aligned} \quad (2)$$

The additive property of information from different sources [41] will be utilized in the proposed transmitter selection strategies. Denoting the (prior) information content associated with a subset of SOPs as $\mathbf{I}_0(\mathbf{x})$ and the information associated with the i th SOP as $\mathbf{I}_i(\mathbf{x})$, the (posterior) information content associated with updating the SOP subset to include the i th SOP is defined as $\mathbf{I}_{\text{posterior},i}(\mathbf{x}) = \mathbf{I}_0(\mathbf{x}) + \mathbf{I}_i(\mathbf{x})$. Appendix B relates the FIM to the horizontal dilution of precision (HDOP) metric, commonly used in positioning and navigation.

ESTIMATION FRAMEWORK

Generally, one needs to estimate the state vector \mathbf{x} , which includes the aerial vehicle's position \mathbf{r}_r and velocity $\dot{\mathbf{r}}_r$ as well as relative clock error states $\{\mathbf{x}_{\text{clk},i}\}_{i=1}^M$ between the vehicle-mounted receiver and each SOP, namely

$$\begin{aligned}\mathbf{x} &\triangleq \left[\mathbf{r}_r^\top, \dot{\mathbf{r}}_r^\top, \Delta\mathbf{x}_{\text{clk},1}^\top, \dots, \Delta\mathbf{x}_{\text{clk},M}^\top \right]^\top \\ \Delta\mathbf{x}_{\text{clk},i} &\triangleq [c \cdot (\delta t_r - \delta t_{s_i}), c \cdot (\dot{\delta t}_r - \dot{\delta t}_{s_i})]^\top.\end{aligned}$$

Formulating the transmitter selection problem with $\mathbf{x} \in \mathbb{R}^{6+2M}$ results in a large-scale optimization problem. To scale down the problem, two simplifications are made. First, it is noted that terrestrial SOPs suffer from poor geometric diversity in the vertical direction (particular as seen by high-altitude aircraft). Therefore, relying exclusively on SOPs for 3D navigation leads to a large vertical dilution of precision [42], [43]. Hence, it is assumed that the aerial vehicle is equipped with an altimeter to determine its altitude. As such, in what follows, the problem is formulated to only consider the 2D (planar) aerial vehicle states. Second, only the position states of the aerial vehicle will be considered, leading to the redefined state vector $\mathbf{x}' \in \mathbb{R}^2$. It will be demonstrated in the “Effect of Timing on the Optimal Transmitter Selection” section that this simplification, which ignores the timing states, results in a negligible increase in position uncertainty (on the order of submeter).

A static, weighted nonlinear least-squares (WNLS) estimator is employed on the redefined state vector \mathbf{x}' . The resulting Jacobian matrix $\mathbf{H}_{\mathbf{r}_r}$ is given by

$$\mathbf{H}_{\mathbf{r}_r} = \begin{bmatrix} \frac{\mathbf{r}_r^\top - \mathbf{r}_{s_1}^\top}{\|\mathbf{r}_r - \mathbf{r}_{s_1}\|_2} \\ \vdots \\ \frac{\mathbf{r}_r^\top - \mathbf{r}_{s_M}^\top}{\|\mathbf{r}_r - \mathbf{r}_{s_M}\|_2} \end{bmatrix}. \quad (3)$$

The WNLS estimation error covariance matrix is given by

$$\mathbf{P}_{\mathbf{r}_r} \triangleq \left[\mathbf{P}_{0,\mathbf{r}_r}^{-1} + \mathbf{H}_{\mathbf{r}_r}^\top \mathbf{R}^{-1} \mathbf{H}_{\mathbf{r}_r} \right]^{-1} \quad (4)$$

where, a prior of \mathbf{x}' may be given, denoted by $\hat{\mathbf{x}'}$, with an associated initial estimation error covariance ($\mathbf{P}_{0,\mathbf{r}_r} = \mathbf{I}_{0,\mathbf{r}_r}^{-1}$) and $\mathbf{R} = \text{diag}[\sigma_{s_1}^2, \dots, \sigma_{s_M}^2]$.

OPTIMAL TRANSMITTER SELECTION PROBLEM

The optimal transmitter selection problem can be cast as the optimization problem

$$\begin{aligned}& \underset{\mathbf{w}}{\text{minimize}} \quad \mathcal{J}(\mathbf{w}) \\ & \text{subject to} \quad \mathbf{1}_M^\top \mathbf{w} = K \\ & \quad w_i \in \{0, 1\}, \quad i = 1, \dots, M\end{aligned}$$

where, $\mathcal{J}(\mathbf{w})$ denotes a desired cost function [e.g., A-, D-, and E-optimality criterion or dilution of precision (DOP) [44], [45]], w_i is a binary decision variable which determines whether to accept or reject the i th measurement, $\mathbf{w} = [w_1, \dots, w_M]^\top$ is a vector of the binary decision variables,

$\mathbf{1}_M \in \mathbb{R}^M$ is a vector of ones, and K is the selection subset's cardinality. This optimization problem is computationally involved to solve in real time due to the integer constraints. Instead of solving the abovementioned optimization problem, two efficient transmitter selection strategies are proposed in the next section.

TRANSMITTER SELECTION FRAMEWORK

The proposed transmitter selection framework selects the most informative SOP subset to minimize the aerial vehicle's position error uncertainty. According to the simplification discussed in the “Estimation Framework” section, only the information contribution from the i th SOP to the position states, denoted $\mathbf{I}_{\mathbf{r}_r,i}$, is used to evaluate the cost function $\mathcal{J}(\mathbf{w})$. Ergo, the cost function is defined as the A-optimality criterion: trace of the posterior position estimation error covariance (equivalently, trace of the inverse of FIM)

$$\begin{aligned}\mathcal{J}(\mathbf{w}) &\triangleq \text{tr} \left[\mathbf{I}_{0,\mathbf{r}_r} + \mathbf{H}_{\mathbf{r}_r}^\top \text{diag}(\mathbf{w}) \mathbf{H}_{\mathbf{r}_r}' \right]^{-1} \\ &= \text{tr} \left[\mathbf{I}_{0,\mathbf{r}_r} + \sum_{i=1}^M w_i \mathbf{I}_{\mathbf{r}_r,i} \right]^{-1}\end{aligned} \quad (5)$$

where, $\mathbf{H}_{\mathbf{r}_r}' \triangleq (\mathbf{R}_a^{-1})^\top \mathbf{H}_{\mathbf{r}_r}$, \mathbf{R}_a is the upper triangular Cholesky factorized measurement covariance (i.e., $\mathbf{R} = \mathbf{R}_a^\top \mathbf{R}_a$), and $\mathbf{I}_{0,\mathbf{r}_r}$ is the prior FIM corresponding to the receiver's position states (see Figure 3).

Algorithm 1 summarizes each of the proposed transmitter selection strategy's steps.

Algorithm 1. Transmitter Selection Strategies

Input: Prior FIM, FIM associated with each measurement, map of all SOPs, and number of SOPs to be selected

Output: SOP selection subset and FIM for the selected SOPs

- 1: Define an empty set for SOP selection
- 2: Perform an exhaustive search to select the two SOPs with the largest information content
- 3: Update the prior FIM and SOP selection subset

One-Shot Selection (OSS)

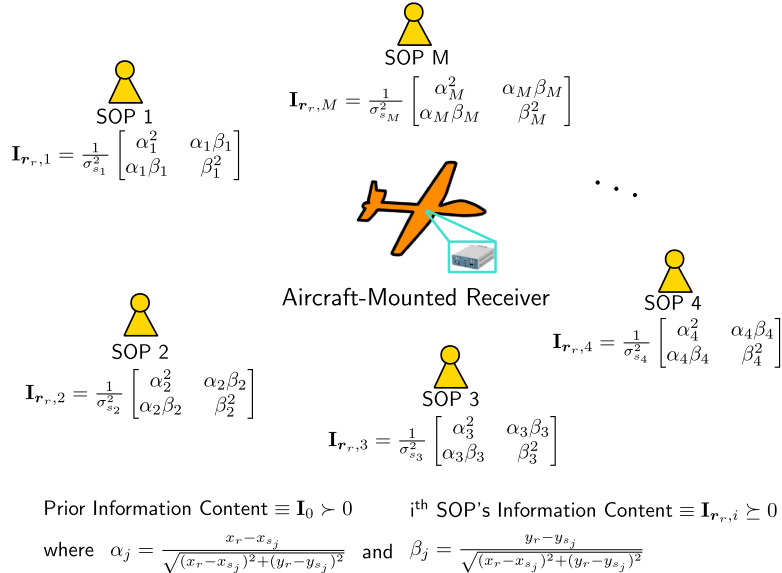
- 4: Compute the posterior FIM for all SOPs, excluding those already selected
- 5: Choose the $K - 2$ SOPs which minimize the receiver's average position error uncertainty
- 6: Compute the FIM for the selected SOPs (i.e., prior FIM plus all selected SOP's FIM) and update the SOP selection subset

- 7: **Return** SOP selection subset and FIM for the selected SOPs

Opportunistic Greedy Selection (OGS)

for $K - 2$ iterations

- 8: Compute the posterior FIM for all SOPs, excluding those already selected
 - 9: Choose one SOP which minimizes the receiver's average position error uncertainty
 - 10: Redefine the prior FIM [i.e., (current) prior FIM plus selected SOP's FIM] and update the SOP selection subset
- end for**


Figure 3.

Receiver estimating its two position states (i.e., $\hat{\mathbf{x}}' \in \mathbb{R}^2$) in an environment comprised of M terrestrial SOPs.

SELECTION STRATEGY ANALYSIS

This section will compare the selection subsets of the proposed transmitter selection strategies and provide an upper bound on the FIM for the selected range-only measurements.

OSS VERSUS OGS SELECTION SUBSET COMPARISON

The OSS and OGS will yield identical selection if the information content is scalar valued, that is, $x \in \mathbb{R}$ is constrained to one dimension. This can be readily shown as follows. First, assume that the posterior FIM $I_{\text{posterior},i} = I_{0,r} + I_{r_r,i}$ are ordered from smallest to largest, such that $\mathcal{J}(I_{\mathbf{w}^1}) \leq \mathcal{J}(I_{\mathbf{w}^2}) \leq \dots \leq \mathcal{J}(I_{\mathbf{w}^K}) \leq \dots \leq \mathcal{J}(I_{\mathbf{w}^M})$, where \mathbf{w}^i is a vector of zeros with a one at the i th element. Therefore, the OSS will yield the optimal selection set $S = \{1, 2, \dots, K\}$, where the information content associated with the selected transmitters is denoted as $\mathbf{I} = \delta_0 + \frac{\xi_1}{\sigma_{s_1}^2} + \dots + \frac{\xi_K}{\sigma_{s_K}^2}$. On the other hand, the OGS recursively selects one transmitter (i.e., $i = 1, \dots, M$), which minimizes the cost function to yield

$$i^* = \operatorname{argmin}_i \left[\gamma_0 + \frac{\xi_3}{\sigma_{s_3}^2} + \frac{\xi_i}{\sigma_{s_i}^2} \right]^{-1}.$$

This selection process is performed at each iteration. By virtue of the simplifying assumption, the minimum argument (resulting in the smallest cost function) is selected in ascending order as $i^* = 4, i^* = 5, \dots, i^* = K$ since $\mathcal{J}(\mathbf{w}^{i^*}) \leq \mathcal{J}(\mathbf{w}^i)$, $\forall i \setminus \{S\}$. Therefore, the transmitter selection subset will be $S = \{1, 2, \dots, K\}$, where the information content associated with the selected transmitters is $I = \delta_0 + \frac{\xi_1}{\sigma_{s_1}^2} + \dots + \frac{\xi_K}{\sigma_{s_K}^2}$, which is identical to the OSS.

For the 2D case, that is, $x \in \mathbb{R}^2$, the OSS and OGS will yield different selections. To show this, one proceeds similarly to the scalar case, noting that in the i th iteration of the OGS

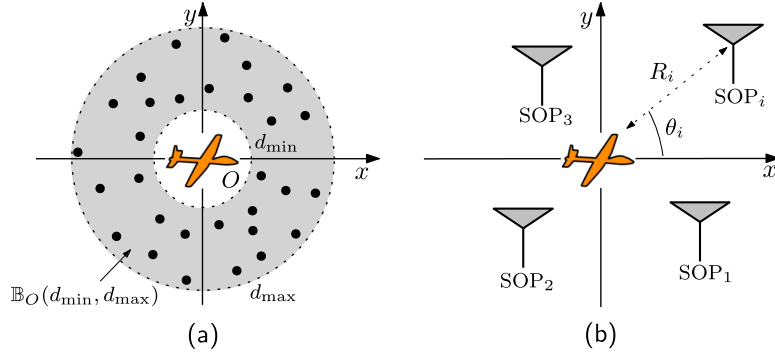
$$i^* = \operatorname{argmin}_{i \notin S} \operatorname{tr} \left(\begin{bmatrix} \gamma'_{11} + \frac{\alpha_1^2}{\sigma_{s_1}^2} & \gamma'_{12} + \frac{\alpha_1\beta_1}{\sigma_{s_1}^2} \\ \gamma'_{12} + \frac{\alpha_1\beta_1}{\sigma_{s_1}^2} & \gamma'_{22} + \frac{\beta_1^2}{\sigma_{s_1}^2} \end{bmatrix}^{-1} \right).$$

This implies that the optimization problem's solution is heavily dependent on the cross terms associated with the i th SOP's posterior FIM. More specifically, each state's information content is coupled with one another. This affects the 2×2 FIM inverse via the determinant term which incorporates the mutually shared information shared (cross terms) between the position state estimates. Therefore, $\mathcal{J}(\mathbf{w}^*) \not\leq \mathcal{J}(\mathbf{w}^i)$, $\forall i \setminus \{S\}$, yielding a different selection subset than the OSS.

COMPUTATIONAL COMPLEXITY OF OSS VERSUS OGS

If one attempts to find the optimal selection strategy by exhaustively searching, that is, M choose K algorithm: $\binom{M}{K} = \frac{M!}{(M-K)!K!}$, the computational complexity is exponential, namely $O(M^K)$ for a large enough M , since $\binom{M}{K} = \frac{M^K}{K!} (1(1 - \frac{1}{M}) \cdots (1 - \frac{K-1}{M}))$ where, K is assumed fixed and $1(1 - \frac{1}{M}) \cdots (1 - \frac{K-1}{M}) \rightarrow 1$ as $M \rightarrow \infty$.

In contrast, the OGS computational complexity is $O(M^2) + O(K-2) \approx O(M^2)$, while the OSS computational complexity is $O(M^2) + O(1) \approx O(M^2)$, for a large enough M , both of which are quadratic. These can be derived by noting that the exhaustive search step's complexity is $\binom{M}{2} = \frac{M^2-M}{2!}$, where $\frac{1}{2!}(M^2 - M) \rightarrow M^2$ as

**Figure 4.**(a) BPP realization with $M = 22$ SOPs. (b) Parameterization of the i th SOP's position.

$M \rightarrow \infty$. For OGS, the recursive search step's computational complexity is defined as $O(K - 2)$ because it requires $K - 2$ iterations to complete. For OSS, the batch selection step's computational complexity is defined as $O(1)$ because it only requires a single iteration to complete.

SIMULATION RESULTS

This section presents simulation results demonstrating the efficacy of the proposed OGS and OSS strategies, which are compared against the optimal selection, whose solution is obtained by exhaustive search $\binom{M}{K}$.

OPTIMAL SELECTION, OSS, AND OGS STRATEGY COMPARISON

The aerial vehicle is assumed to have initial access to GNSS signals, leading to knowledge of its initial position estimates $\hat{\mathbf{r}}_r(0)$, after which the aerial vehicle loses access to GNSS. During GNSS availability, the aerial vehicle chooses the “best” $K < M$ SOPs to use for navigation once GNSS signals are cut off.

The cellular SOP network was modeled as a binomial point process (BPP), where the horizontal positions of the SOPs are independently and uniformly distributed over an annular region centered at the aerial vehicle’s current position O , that is, $\mathbb{B}_O(d_{\min}, d_{\max}) = \pi(d_{\max}^2 - d_{\min}^2)$ [46], where d_{\max} is the maximum distance for which ranging signals can be detected by the receiver and d_{\min} is the minimum distance required for the far-field assumption to hold (see Figure 4). The location of the i th SOP with respect to the aerial vehicle can be parameterized in terms of the range R_i and bearing angle θ_i .

The simulation environment considered $M = 22$ terrestrial SOPs, of which $K \in \{6, 7, \dots, 14\}$ are to be selected. For each K , 10^3 Monte Carlo (MC) realizations were generated according to the simulation settings summarized in Table 1. The randomized MC realizations were the clock’s process noise, measurement noise, and SOPs’

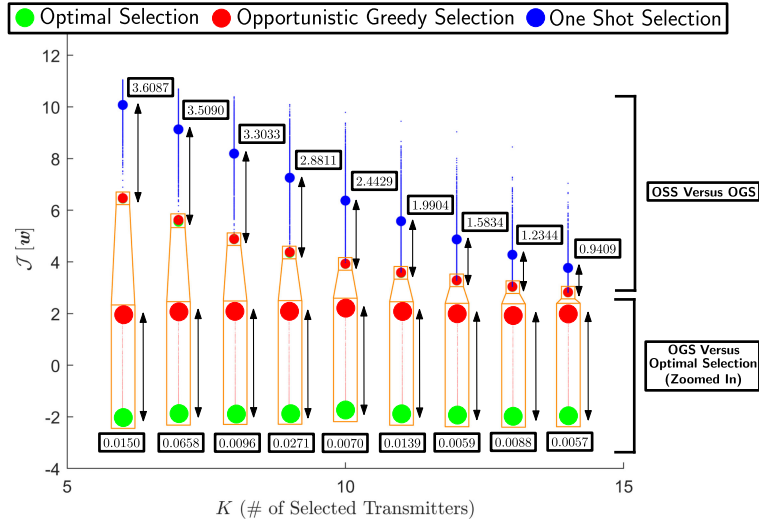
locations. The three selection strategies (optimal, OSS, and OGS) were performed for each realization.

Figure 5 compares the transmitter selection strategy performance for each K . The medium-sized green, blue, and red dots represent the cost function values for the optimal selection $\bar{\mathcal{J}}(\mathbf{w}_*)$, OGS $\bar{\mathcal{J}}(\mathbf{w}_{\text{OGS}})$, and OSS $\bar{\mathcal{J}}(\mathbf{w}_{\text{OSS}})$, respectively, averaged over all MC realizations. The tiny green, blue, and red dots represent the cost function value for each MC realization. It can be seen that, on one hand, the OGS yielded very close solution to the optimal value (the medium green and red dots are nearly on top of each other). The zoom, in the following, shows the difference between both solutions [i.e., $\bar{\mathcal{J}}(\mathbf{w}_*) - \bar{\mathcal{J}}(\mathbf{w}_{\text{OGS}})$]. On the other

Table 1.

Transmitter Selection Environment Simulation Settings

Parameter	Value
M	22
K	{6, 7, ..., 14}
$\mathbf{r}_r(0)$	$[0, 0]^T$
$\mathbf{P}_{0,\mathbf{r}_r}$	$10^2 \cdot \mathbf{I}_{2 \times 2}$
$\hat{\mathbf{r}}_r(0)$	$\sim \mathcal{N}[\mathbf{r}_r(0), \mathbf{P}_{\mathbf{r}_r}]$
$\{R_i, \theta_i\}$	$\{\mathcal{U}[5, 80,000] \text{ m}, \mathcal{U}[-\pi, \pi] \text{ rad}\}$
\mathbf{r}_{s_i}	$[R_i \cos(\theta_i), R_i \sin(\theta_i)]^T$
$\mathbf{x}_{\text{clk},i}(0)$	$c \cdot [9, 0.9]^T$
$\{\mathbf{x}_{s_i}(0)\}_{i=1}^M$	$[\mathbf{r}_{s_i}^T(0), \mathbf{x}_{\text{clk},i}^T(0)]^T$
$\{\mathbf{P}_{0,\text{clk},s_i}\}_{i=1}^M$	$\text{diag}[30 \times 10^3, 0.3 \times 10^3]$
$\{\hat{\mathbf{x}}_{\text{clk},s_i}(0)\}_{i=1}^M$	$\sim \mathcal{N}[\mathbf{x}_{\text{clk},i}(0), \mathbf{P}_{x_{0,\text{clk},s_i}}]$
$\{h_{0,\mathbf{r}}, h_{-2,\mathbf{r}}\}$	$\{8.0 \times 10^{-20}, 4.0 \times 10^{-23}\}$
$\{h_{0,\mathbf{s}_i}, h_{-2,\mathbf{s}_i}\}_{i=1}^M$	$\{2.6 \times 10^{-22}, 4.0 \times 10^{-26}\}$
$\{\sigma_{s_i}^2\}_{i=1}^M$	10 m^2
T	0.01 s


Figure 5.

Cost function point cloud with 10^3 MC realizations for optimal selection (green), OGS (red), and OSS (blue). The average cost function values over all MC realizations is shown as medium-sized dots, while the cost function value for each MC realization is represented as tiny dots. The top boxed values represent $\bar{J}(w_*) - \bar{J}(w_{OSS})$, while bottom boxed values (in the zoomed in) represent $\bar{J}(w_*) - \bar{J}(w_{OGS})$.

hand, the OSS yielded solutions that were further than the optimal solution.

Table 2 shows the average cost function values $\bar{J}(w)$ over all MC realizations along with the corresponding $\pm 1\sigma$. Note that the average cost function values for the OGS and optimal selection strategies are very close to each other with a low standard deviation, whereas the OSS strategy is prone to worse selection performance (i.e., larger cost function value) with a higher standard deviation.

EFFECT OF TIMING ON THE OPTIMAL TRANSMITTER SELECTION

A simulation was conducted to justify the simplification invoked in the “Estimation Framework” section, whereby only the aerial vehicle’s position states were considered, while ignoring the timing states. To this end, 250 MC realizations were generated, for each of which, the optimal transmitter selection strategy $\binom{M}{K}$ was performed to

minimize (5) with the FIM

$$\mathbf{I}(\mathbf{x}') = \mathbf{I}_{0,\mathbf{r}}(\mathbf{x}') + \sum_{i=1}^M \frac{w_i}{\sigma_{s_i}^2} \begin{bmatrix} \alpha_i^2 & \alpha_i \beta_i \\ \alpha_i \beta_i & \beta_i^2 \end{bmatrix}.$$

Next, the FIM that considers the full state vector \mathbf{x} (comprising position, velocity, and timing states) was used to find the optimal selection, that is, minimize (5), but with the FIM

$$\mathbf{I}(\mathbf{x}) = \mathbf{I}_0(\mathbf{x})$$

$$+ \begin{bmatrix} \sum_{i=1}^M \frac{w_i \alpha_i^2}{\sigma_{s_i}^2} & \sum_{i=1}^M \frac{w_i \alpha_i \beta_i}{\sigma_{s_i}^2} & \frac{w_1 \alpha_1}{\sigma_{s_1}^2} & \frac{w_2 \alpha_2}{\sigma_{s_2}^2} & \dots & \frac{w_M \alpha_M}{\sigma_{s_M}^2} \\ \sum_{i=1}^M \frac{w_i \alpha_i \beta_i}{\sigma_{s_i}^2} & \sum_{i=1}^M \frac{w_i \beta_i^2}{\sigma_{s_i}^2} & \frac{w_1 \beta_1}{\sigma_{s_1}^2} & \frac{w_2 \beta_2}{\sigma_{s_2}^2} & \dots & \frac{w_M \beta_M}{\sigma_{s_M}^2} \\ \frac{w_1 \alpha_1}{\sigma_{s_1}^2} & \frac{w_1 \beta_1}{\sigma_{s_1}^2} & \frac{w_1}{\sigma_{s_1}^2} & 0 & 0 & 0 \\ \frac{w_2 \alpha_2}{\sigma_{s_2}^2} & \frac{w_2 \beta_2}{\sigma_{s_2}^2} & 0 & \frac{w_2}{\sigma_{s_2}^2} & 0 & 0 \\ \vdots & \vdots & \vdots & \vdots & \ddots & \vdots \\ \frac{w_K \alpha_K}{\sigma_{s_K}^2} & \frac{w_K \beta_K}{\sigma_{s_K}^2} & 0 & 0 & 0 & \frac{w_K}{\sigma_{s_K}^2} \end{bmatrix}.$$

Table 2.
Average Cost Function Values for the Transmitter Selection Strategies with $K = 6 - 14$

K	6	7	8	9	10	11	12	13	14
$\bar{J}(w_*)$ [$\pm \sigma_*$]	6.45 [± 0.001]	5.56 [± 0.005]	4.88 [± 0.006]	4.35 [± 0.009]	3.92 [± 0.01]	3.57 [± 0.01]	3.28 [± 0.01]	3.03 [± 0.02]	2.82 [± 0.02]
$\bar{J}(w_{OSS})$ [$\pm \sigma_{OSS}$]	6.47 [± 0.02]	5.62 [± 0.02]	4.89 [± 0.01]	4.38 [± 0.01]	3.93 [± 0.01]	3.59 [± 0.02]	3.29 [± 0.02]	3.04 [± 0.02]	2.83 [± 0.03]
$\bar{J}(w_{OGS})$ [$\pm \sigma_{OGS}$]	10.08 [± 0.76]	9.13 [± 0.99]	8.19 [± 1.13]	7.26 [± 1.19]	6.37 [± 1.16]	5.58 [± 1.08]	4.87 [± 0.96]	4.28 [± 0.84]	3.77 [± 0.70]

Table 3.

K	6	7	8	9	10	11	12	13	14
Uncertainty reduction [m ²]	0.2630	0.2593	0.2643	0.2568	0.2862	0.2183	0.2781	0.2178	0.2475

Table 3 tabulates the reduction in position uncertainty (averaged over all MC realizations for each K value) upon including the timing error states in the FIM. It can be noted that the reduction in position uncertainty is small (on the order of submeter), which justifies the considered simplification.

EXPERIMENTAL RESULTS

This section demonstrates the efficacy of the proposed algorithms to select a “manageable” subset of terrestrial SOPs to navigate an aircraft in a real-world environment.

HARDWARE AND SOFTWARE SETUP

The SNIFFER flight campaign took place on a Beechcraft C12 Huron (called Ms. Mabel), a fixed-wing U.S. Air Force aircraft, flown by members of the USAF Test Pilot School (TPS) over two different regions as follows. i) A rural region located in Edwards, California, USA. ii) A semiurban region located in Palmdale, California, USA.

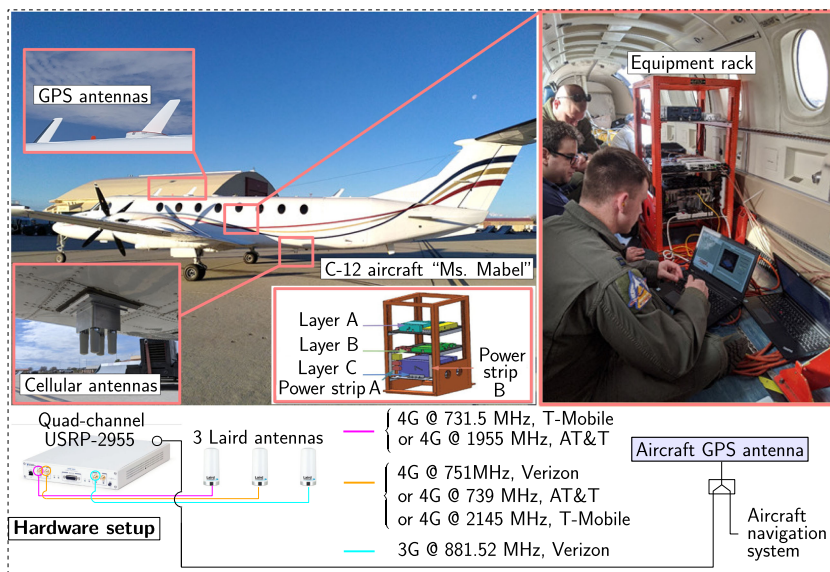
The C-12 aircraft was equipped with a quad-channel universal software radio peripheral (USRP)-2955, three

consumer-grade 800/1900 MHz Laird cellular antennas, GPS antenna, a solid-state drive for data storage, PCIe cable, and a laptop computer running ASPIN Laboratory’s software-defined radio (SDR), called MATRIX: Multi-channel Adaptive TRansceiver Information eXtractor, for real-time monitoring of the cellular signals [27]. The MATRIX SDR produced the navigation observables: Doppler frequency, carrier phase, and pseudorange, along with the corresponding carrier-to-noise ratio (C/N_0). The experimental hardware setup is shown in Figure 6.

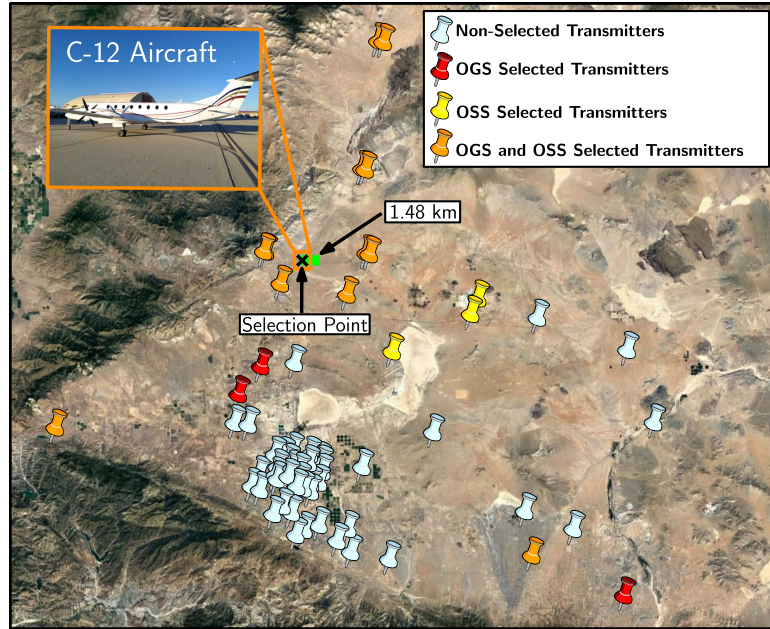
TRANSMITTER SELECTION AND NAVIGATION FILTER

The OGS and OSS selection strategies were performed in each of the two regions. To demonstrate the efficacy of the selected transmitters for aircraft navigation, the pseudorange measurements from the selected transmitters are fused with altimeter measurements via an extended Kalman filter (EKF), as described in [27]. The navigation solution was computed over a flight segment during which the selection strategies remained valid.

The EKF’s initial state vector was set as $\hat{\mathbf{x}}(0) = [\hat{\mathbf{r}}_r(0)^T, \dot{\hat{\mathbf{r}}}_r(0)^T, c \delta t_1(0), c\dot{\delta}t_1(0), \dots, c\delta t_K(0), c\dot{\delta}t_K(0)]^T$ with a corresponding initial estimation error

**Figure 6.**

Hardware setup equipped to the C-12 aircraft.

**Figure 7.**

Rural region transmitter selection results with OGS and OSS strategies during the aircraft's flight. (Map data: Google Earth.)

covariance $\mathbf{P}(0) = \text{diag}[10^2 \cdot \mathbf{I}_{3 \times 3}, 10 \cdot \mathbf{I}_{3 \times 3}, 10^8, 10, \dots, 10^8, 10]$. The clock error states of each SOP was initialized using the pseudorange measurements from the initial two time epochs. Specifically, the clock bias was initialized as $c\hat{\delta}t_i(0) = z_{s_i}(0) - \|\mathbf{r}_r(0) - \mathbf{r}_{s_i}\|_2$ and the clock drift was initialized as $c\dot{\hat{\delta}}t_i(0) = \frac{1}{T}[z_{s_i}(1) - z_{s_i}(0) - \|\mathbf{r}_r(1) - \mathbf{r}_{s_i}\|_2 + \|\mathbf{r}_r(0) - \mathbf{r}_{s_i}\|_2]$.

The aircraft's dynamics was assumed to evolve according to the simple, yet effective, velocity random walk model [47], with power spectra of the continuous-time acceleration noise in the East (E), North (N), and Up (U) directions set as $\tilde{q}_E = \tilde{q}_N = 5 \text{ m}^2/\text{s}^3$ and $\tilde{q}_U = 10^{-3} \text{ m}^2/\text{s}^3$, respectively.

The receiver's clock covariance $\mathbf{Q}_{\text{clk},r}$ was set to correspond to a low-quality temperature-compensated crystal oscillator (TCXO) with $h_{0,r} = 2.0 \times 10^{-19} \text{ s}$ and $h_{-2,r} = 2.0 \times 10^{-20} \text{ s}^{-1}$. The SOPs' clock covariance $\mathbf{Q}_{\text{clk},s_i}$ was set to correspond to a typical-quality oven-controlled crystal oscillator with $h_{0,s_i} = 8.0 \times 10^{-20} \text{ s}$ and $h_{-2,s_i} =$

$4.0 \times 10^{-23} \text{ s}^{-1}$. The time-varying measurement covariance \mathbf{R} was proportional to the inverse of C/N_0 and the sampling time was $T = 0.01 \text{ s}$.

FLIGHT REGION I: RURAL

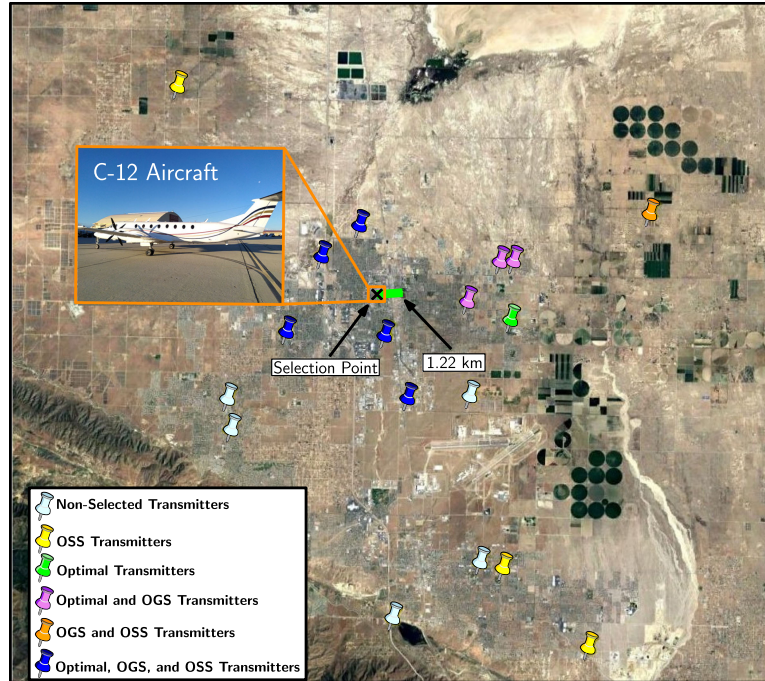
The rural region was comprised of $M = 57$ terrestrial cellular SOPs, where the aircraft was tasked with selecting the most “informative” $K = 15$ SOPs to use for navigation.

Figure 7 shows: i) selected SOPs from OGS (red pins), ii) selected SOPs from OSS (yellow pins), iii) selected SOPs from both OSS and OGS strategies (orange pins), and iv) nonselected SOPs (white pins). Table 6 compares the snapshot performance (A-, D-, and E-optimality and HDOP metrics) of the OGS versus OSS selection.

Upon selecting the SOPs, the aircraft navigated along the green trajectory in Figure 7 for 1.48 km. It should be noted the optimal solution (i.e., global minimizer) for

Table 4.**Experiment I: Navigation Solution Performance in the Rural Region**

Selection Type	Pos. RMSE [m]	Vel. RMSE [m/s]	Max pos. error [m]	Max vel. error [m/s]	Run time [ms]
10^5 MC Runs	[4.53, 71.55]	[0.98, 7.61]	[10.50, 125.06]	[5.90, 11.46]	–
OGS	6.28	1.44	10.50	6.38	19.30
OSS	7.13	1.39	10.50	6.38	16.50

**Figure 8.**

Semiurban region transmitter selection results with optimal selection, OGS, and OSS strategies during the aircraft's flight. (Map data: Google Earth.)

terrestrial SOP selection is infeasible to compute using the $\binom{M}{K}$ selection strategy due to its formidable run time. In light of this, 10^5 MC runs were performed in an attempt to capture a range of best-to-worst selections. Table 4 summarizes the navigation performance when using the transmitters selected by the OGS, OSS, and MC realizations. It is worth noting that the OGS returned relatively comparable performance to the best-case MC realization. It is also worth noting the worst-case MC realization yielding much larger error than the best-case realization (i.e., the variance is rather large), which further motivates the importance of transmitter selection.

FLIGHT REGION 2: SEMIURBAN

The semiurban region was comprised of $M = 18$ terrestrial cellular SOPs, where the aircraft was tasked with

selecting the most "informative" $K = 9$ SOPs to use for navigation.

The number of SOPs in this region was small enough to compute the optimal solution via the $\binom{M}{K}$ selection strategy to determine the global minimizer. Figure 8 shows: i) selected SOPs from $\binom{M}{K}$ (green pins), ii) selected SOPs from OGS (violet pins), iii) selected SOPs from OSS (yellow pins), iv) selected SOPs from both OSS and OGS strategies (orange pins), v) nonselected SOPs (white pins). Table 7 compares the snapshot performance (A-, D-, and E-optimality and HDOP metrics) of the optimal versus OGS and OSS.

Upon selecting the SOPs, the aircraft navigated along the green trajectory in Figure 8 for 1.22 km. Table 5 summarizes the navigation performance when using the transmitters selected by the optimal, OGS, and OSS. Note that the navigation performance with the OGS strategy is close

Table 5.

Experiment 2: Navigation Solution Performance in the Semiurban Region					
Selection type	Pos. RMSE [m]	Vel. RMSE [m/s]	Max pos. error [m]	Max vel. error [m/s]	Run time [ms]
Optimal Selection	5.84	1.45	10.80	5.90	700.30
OGS	6.08	1.42	10.80	5.90	5.30
OSS	6.70	1.35	10.80	5.90	3.90

Table 6.

Experiment 1: Snapshot Performance Metrics in Rural Region After Transmitter Selection				
Selection type	$\text{tr}[\mathbf{P}_{\mathbf{r}_r}]$	$\log[\det(\mathbf{P}_{\mathbf{r}_r})]$	$\lambda_{\max}[\mathbf{P}_{\mathbf{r}_r}]$	HDOP
OGS	200.99	9.20	100.00	0.54
OSS	200.99	9.20	100.00	0.54

Table 7.

Experiment 2: Snapshot Performance Metrics in Semiurban Region After Transmitter Selection				
Selection type	$\text{tr}[\mathbf{P}_{\mathbf{r}_r}]$	$\log[\det(\mathbf{P}_{\mathbf{r}_r})]$	$\lambda_{\max}[\mathbf{P}_{\mathbf{r}_r}]$	HDOP
Optimal selection	200.99	9.20	100.00	0.74
OGS	200.99	9.20	100.00	0.88
OSS	200.99	9.20	100.00	0.94

to that of the optimal selection, whereas the OSS strategy performed slightly worse. This further motivates using the computationally efficient OGS selection strategy instead of the computationally expensive optimal selection strategy, over this valid selection region.

CONCLUSION

This article proposed computationally efficient transmitter selection strategies to select the most informative terrestrial SOPs to use when navigating an aerial vehicle. The strategies exploited the additive, iterative properties of the FIM to minimize the vehicle's average position error variance. Simulation results showed the OGS performance to be very close to the optimal selection, while executing in a fraction of the optimal selection's time. Experimental results in a real-world environment were presented showing the efficacy of the OGS and OSS strategies in navigating a U.S. Air Force high-altitude aircraft with terrestrial cellular SOPs. The achieved position RMSE with the optimal, OGS, and OSS solutions were 4.53, 6.28, and 7.13 m in the rural region; and 5.83, 6.08, and 6.70 m in the semiurban region for an aircraft traversing a trajectory of 1.48 and 1.22 km, respectively.

APPENDIX A

CLOCK ERROR DYNAMICS

The aerial vehicle-mounted receiver's and SOP's clock error states are assumed to evolve according to

$$\mathbf{x}_{\text{clk}}(k+1) = \mathbf{F}_{\text{clk}} \mathbf{x}_{\text{clk}}(k) + \mathbf{w}_{\text{clk}}(k) \quad (6)$$

$$\mathbf{x}_{\text{clk}} \triangleq [c\delta t, c\dot{\delta}t]^T, \quad \mathbf{F}_{\text{clk}} = \begin{bmatrix} 1 & T \\ 0 & 1 \end{bmatrix}$$

where, δt is the clock bias, $\dot{\delta}t$ is the clock drift, c is the speed of light, T is the constant sampling interval, and \mathbf{w}_{clk} is the process noise, which is modeled as a discrete-time white noise sequence with covariance

$$\mathbf{Q}_{\text{clk}} = c^2 \cdot \begin{bmatrix} S_{\bar{w}_{\delta t}} T + S_{\bar{w}_{\delta t}} \frac{T^3}{3} & S_{\bar{w}_{\delta t}} \frac{T^2}{2} \\ S_{\bar{w}_{\delta t}} \frac{T^2}{2} & S_{\bar{w}_{\delta t}} T \end{bmatrix}. \quad (7)$$

The terms $S_{\bar{w}_{\delta t}}$ and $S_{\bar{w}_{\dot{\delta}t}}$ are the clock bias and drift process noise power spectral densities, respectively, which can be related to the power-law coefficients, $\{h_{\alpha_i}\}_{\alpha_i=-2}^2$, which have been shown through laboratory experiments to characterize the power spectral density (PSD) of the fractional frequency deviation of an oscillator from nominal frequency according to $S_{\bar{w}_{\delta t}} \approx \frac{h_0}{2}$ and $S_{\bar{w}_{\dot{\delta}t}} \approx 2\pi^2 h_{-2}$.

The receiver's and SOPs' process noise covariances $\mathbf{Q}_{\text{clk},r}$ and $\{\mathbf{Q}_{\text{clk},s_i}\}_{i=1}^M$ are calculated from (7) using the PSDs associated with the receiver's and SOPs' oscillator quality, respectively.

APPENDIX B

RELATIONSHIP BETWEEN WEIGHTED HDOP AND INFORMATION CONTENT

DOP states how errors in the measurement will affect errors in the final estimates of the unknown quantities. The weighted HDOP matrix for the measurement vector $\mathbf{z}' \triangleq [z'_{s_1}, \dots, z'_{s_M}]^T$ with an associated Jacobian matrix

\mathbf{H} defined in (3) and measurement covariance $\mathbf{R} = \text{diag}[\sigma_{s_1}^2, \dots, \sigma_{s_M}^2]$, is defined as $\mathbf{D}_w \triangleq [\mathbf{H}^\top \mathbf{R}^{-1} \mathbf{H}]^{-1}$, which has the form

$$\mathbf{D}_w = \begin{bmatrix} \sigma_x^2 & \sigma_{xy}^2 \\ \sigma_{xy}^2 & \sigma_y^2 \end{bmatrix}. \quad (8)$$

The weighted HDOP is $\sqrt{\text{tr}(\mathbf{D}_w)} = \sqrt{\sigma_x^2 + \sigma_y^2}$ [48].

The weighted HDOP matrix can be related to information content by the inverse of the estimation error covariance matrix as

$$\begin{aligned} \mathbf{D}_w^{-1} &= \sum_{j=1}^K \frac{1}{\sigma_{s_j}^2} \begin{bmatrix} \frac{(x_r - x_{s_j})^2}{(x_r - x_{s_j})^2 + (y_r - y_{s_j})^2} & \frac{(x_r - x_{s_j})(y_r - y_{s_j})}{(x_r - x_{s_j})^2 + (y_r - y_{s_j})^2} \\ \frac{(x_r - x_{s_j})(y_r - y_{s_j})}{(x_r - x_{s_j})^2 + (y_r - y_{s_j})^2} & \frac{(y_r - y_{s_j})^2}{(x_r - x_{s_j})^2 + (y_r - y_{s_j})^2} \end{bmatrix} \\ &= \sum_{j=1}^K \frac{1}{\sigma_{s_j}^2} \begin{bmatrix} \alpha_j^2 & \alpha_j \beta_j \\ \alpha_j \beta_j & \beta_j^2 \end{bmatrix} \end{aligned}$$

where, α_j and β_j are variables which define the position unit vectors (i.e., $[\alpha_j, \beta_j]^\top = \frac{\mathbf{r}_r - \mathbf{r}_{s_j}}{\|\mathbf{r}_r - \mathbf{r}_{s_j}\|_2}$).

In addition, the weighted HDOP matrix can be related to the information content in a closed form, defined by

$$\mathbf{D}_w = \Lambda \sum_{j=1}^K \frac{1}{\sigma_{s_j}^2} \begin{bmatrix} \beta_j^2 & -\alpha_j \beta_j \\ -\alpha_j \beta_j & \alpha_j^2 \end{bmatrix} \quad (9)$$

where

$$\Lambda = \left[\left\{ \sum_{j=1}^K \frac{\alpha_j^2}{\sigma_{s_j}^2} \right\} \left\{ \sum_{j=1}^K \frac{\beta_j^2}{\sigma_{s_j}^2} \right\} - \left\{ \sum_{j=1}^K \frac{\alpha_j \beta_j}{\sigma_{s_j}^2} \right\}^2 \right]^{-1}$$

is a constant value, corresponding to the information content of the position states, which is found in all HDOP terms. Finally, the HDOP constant can be defined as

$$\text{HDOP} = \sqrt{\Lambda \left\{ \sum_{j=1}^K \frac{1}{\sigma_{s_j}^2} (\beta_j^2 + \alpha_j^2) \right\}}. \quad (10)$$

ACKNOWLEDGMENTS

The authors would like to thank Ali Abdallah for his help with data processing as well as Tucker Haydon, Nadim Khairallah, and Mohammad Neinavaie for helpful discussions. The authors would like to thank Edwards Air Force Base (AFB) and Holloman AFB for inviting the ASPIN Laboratory to conduct experiments on U.S. Air Force aircraft in the “SNIFFER: Signals of opportunity for Navigation In Frequency-Forbidden Environments” flight campaign. The authors would like to thank the U.S. Air Force pilots Chiawei Lee, Juan Jurado, Steven Wachtel, Jacob Duede, Zachary Hoeffner, Thomas Hulsey, and Rachel Quirarte and Republic of Singapore Air Force pilot RunXuan Tay. The authors would also like to thank Joe

Khalife, Joshua Morales, Kimia Shamaei, Mahdi Maaref, Kyle Semelka, MyLinh Nguyen, and Trier Mortlock for their help with preparing for data collection. DISTRIBUTION STATEMENT A. Approved for public release; Distribution is unlimited. 412TW-PA-20146. This work was supported in part by the National Science Foundation (NSF) under Grant 1929571, and in part by the Air Force Office of Scientific Research (AFOSR) under Grant FA9550-22-1-0476. This work was also supported in part by the Laboratory Directed Research and Development program at Sandia National Laboratories, a multi-mission laboratory managed and operated by National Technology and Engineering Solutions of Sandia LLC, a wholly owned subsidiary of Honeywell International Inc. for the U.S. Department of Energy’s National Nuclear Security Administration, under contract DENA0003525. This paper describes objective technical results and analysis. Any subjective views or opinions that might be expressed in the paper do not necessarily represent the views of the U.S. Department of Energy or the United States Government. SAND2022-13901 C.

REFERENCES

- [1] R. Sabatini et al., “Avionics systems panel research and innovation perspectives,” *IEEE Aerosp. Electron. Syst. Mag.*, vol. 35, no. 12, pp. 58–72, Dec. 2020, doi: [10.1109/MAES.2020.3033475](https://doi.org/10.1109/MAES.2020.3033475).
- [2] EUROCONTROL, Aviation Intelligence Unit, “Does radio frequency interference to satellite navigation pose an increasing threat to network efficiency, cost-effectiveness and ultimately safety?,” Tech. Rep., Mar. 2021. [Online]. Available: <https://www.eurocontrol.int/sites/default/files/2021-03/eurocontrol-think-paper-9-radio-frequency-interference-satellite-navigation.pdf>
- [3] International Civil Aviation Organization (ICAO), “An urgent need to address harmful interferences to GNSS,” Tech. Rep., May 2019. [Online]. Available: <https://www.iata.org/contentassets/e45e5219cc8c4277a0e80562590793da/address-harmful-interferences-gnss.pdf>
- [4] J. Raquet et al., “Part D: Position, navigation, and timing using radio signals-of-opportunity,” *Position, Navigation, and Timing Technologies in the 21st Century*, J. Morton, F. van Diggelen, J. Spilker Jr., and B. Parkinson, Eds. New York, NY, USA: Wiley, 2021, vol. 2, ch. 35–43, pp. 1115–1412, doi: [10.1002/9781119458555.ch35](https://doi.org/10.1002/9781119458555.ch35).
- [5] J. Mortier, G. Pages, and J. Vila-Valls, “Robust TOA-based UAS navigation under model mismatch in GNSS-denied harsh environments,” *Remote Sens.*, vol. 12, no. 18, pp. 2928–2947, Sep. 2020, doi: [10.3390/rs12182928](https://doi.org/10.3390/rs12182928).
- [6] N. Souli, P. Kolios, and G. Ellinas, “Online relative positioning of autonomous vehicles using signals of opportunity,” *IEEE Trans. Intell. Veh.*, vol. 7, no. 4, pp. 873–885, Dec. 2022, doi: [10.1109/TIV.2021.3124727](https://doi.org/10.1109/TIV.2021.3124727).

- [7] Z. Kassas, J. Khalife, A. Abdallah, and C. Lee, "I am not afraid of the GPS jammer: Resilient navigation via signals of opportunity in GPS-denied environments," *IEEE Aerosp. Electron. Syst. Mag.*, vol. 37, no. 7, pp. 4–19, Jul. 2022, doi: [10.1109/MAES2022.3154110](https://doi.org/10.1109/MAES2022.3154110).
- [8] M. Psiaki and B. Slosman, "Tracking of digital FM OFDM signals for the determination of navigation observables," in *Proc. ION GNSS Conf.*, 2019, pp. 2325–2348, doi: [10.33012/2019.17120](https://doi.org/10.33012/2019.17120).
- [9] X. Chen, Q. Wei, F. Wang, Z. Jun, S. Wu, and A. Men, "Super-resolution time of arrival estimation for a symbiotic FM radio data system," *IEEE Trans. Broadcast.*, vol. 66, no. 4, pp. 847–856, Dec. 2020, doi: [10.1109/TBC.2019.2957666](https://doi.org/10.1109/TBC.2019.2957666).
- [10] K. Shamaei and Z. Kassas, "Receiver design and time of arrival estimation for opportunistic localization with 5 G signals," *IEEE Trans. Wireless Commun.*, vol. 20, no. 7, pp. 4716–4731, Jul. 2021, doi: [10.1109/TWC.2021.3061985](https://doi.org/10.1109/TWC.2021.3061985).
- [11] P. Wang, Y. Wang, and J. Morton, "Signal tracking algorithm with adaptive multipath mitigation and experimental results for LTE positioning receivers in urban environments," *IEEE Trans. Aerosp. Electron. Syst.*, vol. 58, no. 4, pp. 2779–2795, Aug. 2022, doi: [10.1109/TAES.2021.3139569](https://doi.org/10.1109/TAES.2021.3139569).
- [12] I. Lapin, G. Granados, J. Samson, O. Renaudin, F. Zanier, and L. Ries, "STARE: Real-time software receiver for LTE and 5 G NR positioning and signal monitoring," in *Proc. Workshop Satell. Navigation Technol.*, 2022, pp. 1–11, doi: [10.1109/NAVITEC53682.2022.9847544](https://doi.org/10.1109/NAVITEC53682.2022.9847544).
- [13] C. Yang, M. Arizabaleta-Diez, P. Weitkemper, and T. Pany, "An experimental analysis of cyclic and reference signals of 4G LTE for TOA estimation and positioning in mobile fading environments," *IEEE Aerosp. Electron. Syst. Mag.*, vol. 37, no. 9, pp. 16–41, Sep. 2022, doi: [10.1109/MAES2022.3186650](https://doi.org/10.1109/MAES2022.3186650).
- [14] C. Yang and A. Soloviev, "Mobile positioning with signals of opportunity in urban and urban canyon environments," in *Proc. IEEE/ION Position, Location, Navigation Symp.*, 2020, pp. 1043–1059, doi: [10.1109/PLANS46316.2020.9109876](https://doi.org/10.1109/PLANS46316.2020.9109876).
- [15] T. Hong, J. Sun, T. Jin, Y. Yi, and J. Qu, "Hybrid positioning with DTMB and LTE signals," in *Proc. Int. Wireless Commun. Mobile Comput.*, 2021, pp. 303–307, doi: [10.1109/IWCMC51323.2021.9498758](https://doi.org/10.1109/IWCMC51323.2021.9498758).
- [16] Z. Kassas, N. Khairallah, and S. Kozhaya, "Ad Astra: Simultaneous tracking and navigation with megaconstellation LEO satellites," *IEEE Aerosp. Electron. Syst. Mag.*, 2023.
- [17] M. Hartnett, "Performance assessment of navigation using carrier Doppler measurements from multiple LEO constellations," Master's thesis, Air Force Institute of Technology, Wright-Patterson AFB, OH, USA, 2022.
- [18] C. Huang, H. Qin, C. Zhao, and H. Liang, "Phase - time method: Accurate doppler measurement for iridium NEXT signals," *IEEE Trans. Aerosp. Electron. Syst.*, vol. 58, no. 6, pp. 5954–5962, Dec. 2022, doi: [10.1109/TAES2022.3180702](https://doi.org/10.1109/TAES2022.3180702).
- [19] J. Khalife and Z. Kassas, "Opportunistic UAV navigation with carrier phase measurements from asynchronous cellular signals," *IEEE Trans. Aerosp. Electron. Syst.*, vol. 56, no. 4, pp. 3285–3301, Aug. 2020, doi: [10.1109/TAES.2019.2948452](https://doi.org/10.1109/TAES.2019.2948452).
- [20] J. Khalife and Z. Kassas, "On the achievability of sub-meter-accurate UAV navigation with cellular signals exploiting loose network synchronization," *IEEE Trans. Aerosp. Electron. Syst.*, vol. 58, no. 5, pp. 4261–4278, Oct. 2022, doi: [10.1109/TAES.2022.3162770](https://doi.org/10.1109/TAES.2022.3162770).
- [21] J. Khalife and Z. Kassas, "Differential framework for sub-meter-accurate vehicular navigation with cellular signals," *IEEE Trans. Intell. Veh.*, vol. 8, no. 1, pp. 732–744, Jan. 2023, doi: [10.1109/TAES.2022.3162770](https://doi.org/10.1109/TAES.2022.3162770).
- [22] N. Schneckenburger et al., "Measurement of the l-band air-to-ground channel for positioning applications," *IEEE Trans. Aerosp. Electron. Syst.*, vol. 52, no. 5, pp. 2281–2297, Oct. 2016, doi: [10.1109/TAES.2016.150451](https://doi.org/10.1109/TAES.2016.150451).
- [23] W. Khawaja, I. Guvenc, D. Matolak, U. Fiebig, and N. Schneckenburger, "A survey of air-to-ground propagation channel modeling for unmanned aerial vehicles," *IEEE Commun. Surv. Tut.*, vol. 21, no. 3, pp. 2361–2391, Jul.–Sep. 2019, doi: [10.1109/COMST.2019.2915069](https://doi.org/10.1109/COMST.2019.2915069).
- [24] E. Kim and Y. Shin, "Feasibility analysis of LTE-based UAS navigation in deep urban areas and DSRC augmentation," *Sensors*, vol. 19, no. 9, pp. 4192–4207, Apr. 2019, doi: [10.3390/s19194192](https://doi.org/10.3390/s19194192).
- [25] B. Stevens and M. Younis, "Detection algorithm for cellular synchronization signals in airborne applications," *IEEE Access*, vol. 9, pp. 55555–55566, Apr. 2021, doi: [10.1109/ACCESS.2021.3071674](https://doi.org/10.1109/ACCESS.2021.3071674).
- [26] Z. Kassas et al., "Received power characterization of terrestrial cellular signals on high altitude aircraft," in *Proc. IEEE Aerosp. Conf.*, 2022, pp. 1–8, doi: [10.1109/AERO53065.2022.9843492](https://doi.org/10.1109/AERO53065.2022.9843492).
- [27] Z. Kassas et al., "Assessment of cellular signals of opportunity for high-altitude aircraft navigation," *IEEE Aerosp. Electron. Syst. Mag.*, vol. 37, no. 10, pp. 4–19, Oct. 2022, doi: [10.1109/MAES.2022.3187142](https://doi.org/10.1109/MAES.2022.3187142).
- [28] Z. Kassas et al., "Protecting the skies: GNSS-less accurate aircraft navigation with terrestrial cellular signals of opportunity," in *Proc. ION GNSS Conf.*, 2022, pp. 1014–1025, doi: [10.33012/2022.18579](https://doi.org/10.33012/2022.18579).
- [29] L. Kaplan, "Local node selection for localization in a distributed sensor network," *IEEE Trans. Aerosp. Electron. Syst.*, vol. 42, no. 1, pp. 136–146, Jan. 2006, doi: [10.1109/TAES.2006.1603410](https://doi.org/10.1109/TAES.2006.1603410).

- [30] N. Cao, S. Choi, E. Masazade, and P. Varshney, "Sensor selection for target tracking in wireless sensor networks with uncertainty," *IEEE Trans. Signal Process.*, vol. 64, no. 20, pp. 5191–5204, Oct. 2016, doi: [10.1109/TSP.2016.2595500](https://doi.org/10.1109/TSP.2016.2595500).
- [31] S. Joshi and S. Boyd, "Sensor selection via convex optimization," *IEEE Trans. Signal Process.*, vol. 57, no. 2, pp. 451–462, Feb. 2009, doi: [10.1109/TSP.2008.2007095](https://doi.org/10.1109/TSP.2008.2007095).
- [32] V. Kekatos and G. Giannakis, "Selecting reliable sensors via convex optimization," in *Proc. IEEE Int. Workshop Signal Process. Adv. Wireless Commun.*, 2010, pp. 1–5, doi: [10.1109/SPAWC.2010.5670891](https://doi.org/10.1109/SPAWC.2010.5670891).
- [33] S. Liu, S. Chepuri, M. Fardad, E. Masazade, G. Leus, and P. Varshney, "Sensor selection for estimation with correlated measurement noise," *IEEE Trans. Signal Process.*, vol. 64, no. 13, pp. 3509–3522, Jul. 2016, doi: [10.1109/TSP.2016.2550005](https://doi.org/10.1109/TSP.2016.2550005).
- [34] Z. Dai, G. W. X. Jin, and X. Lou, "Nearly optimal sensor selection for TDOA-based source localization in wireless sensor networks," *IEEE Trans. Veh. Technol.*, vol. 69, no. 10, pp. 12031–12042, Oct. 2020, doi: [10.1109/TVT.2020.3011118](https://doi.org/10.1109/TVT.2020.3011118).
- [35] V. Cerone, S. Fosson, and D. Regruto, "A non-convex adaptive regularization approach to binary optimization," in *Proc. IEEE Conf. Decis. Control*, 2021, pp. 3844–3849, doi: [10.1109/CDC45484.2021.9683667](https://doi.org/10.1109/CDC45484.2021.9683667).
- [36] A. Hashemi, M. Ghasemi, H. Vikalo, and U. Topcu, "Randomized greedy sensor selection: Leveraging weak submodularity," *IEEE Trans. Autom. Control*, vol. 66, no. 1, pp. 199–212, Jan. 2021, doi: [10.1109/TAC.2020.2980924](https://doi.org/10.1109/TAC.2020.2980924).
- [37] Y. Saito et al., "Determinant-based fast greedy sensor selection algorithm," *IEEE Access*, vol. 9, pp. 68535–68551, 2021, doi: [10.1109/ACCESS.2021.3076186](https://doi.org/10.1109/ACCESS.2021.3076186).
- [38] X. Shen and P. Varshney, "Sensor selection based on generalized information gain for target tracking in large sensor networks," *IEEE Trans. Signal Process.*, vol. 62, no. 2, pp. 363–375, Jan. 2014, doi: [10.1109/TSP.2013.2289881](https://doi.org/10.1109/TSP.2013.2289881).
- [39] F. Wang, X. Bai, B. Guo, and C. Liu, "Dynamic clustering in wireless sensor network for target tracking based on the fisher information of modified kalman filter," in *Proc. IEEE Int. Conf. Syst. Informat.*, 2016, pp. 696–700, doi: [10.1109/ICSAI2016.7811042](https://doi.org/10.1109/ICSAI2016.7811042).
- [40] A. Nguyen and Z. Kassas, "Transmitter selection for improved information gathering in aerial vehicle navigation with terrestrial signals of opportunity," in *Proc. ION Int. Tech. Meeting*, 2022, pp. 723–734, doi: [10.33012/2022.18262](https://doi.org/10.33012/2022.18262).
- [41] G. Mutambara, *Decentralized Estimation and Control for Multisensor Systems*. Boca Raton, FL, USA: CRC Press, 1998.
- [42] J. Morales, J. Khalife, and Z. Kassas, "Opportunity for accuracy," *GPS World Mag.*, vol. 27, no. 3, pp. 22–29, Mar. 2016.
- [43] M. Maaref, J. Khalife, and Z. Kassas, "Aerial vehicle protection level reduction by fusing GNSS and terrestrial signals of opportunity," *IEEE Trans. Intell. Transp. Syst.*, vol. 22, no. 9, pp. 5976–5993, Sep. 2021, doi: [10.1109/TITS.2021.3095184](https://doi.org/10.1109/TITS.2021.3095184).
- [44] D. Uciński, *Optimal Measurement Methods for Distributed Parameter System Identification*. Boca Raton, FL, USA: CRC Press, 2005.
- [45] N. Blanco-Delgado, F. Nunes, and G. Seco-Granados, "Relation between GDOP and the geometry of the satellite constellation," in *Int. Conf. Localization GNSS*, 2011, pp. 175–180, doi: [10.1109/ICL-GNSS.2011.5955282](https://doi.org/10.1109/ICL-GNSS.2011.5955282).
- [46] S. Aditya, H. Dhillon, A. Molisch, R. Buehrer, and H. Behairy, "Characterizing the impact of SNR heterogeneity on time-of-arrival-based localization outage probability," *IEEE Trans. Wireless Commun.*, vol. 18, no. 1, pp. 637–649, Jan. 2019, doi: [10.1109/TWC.2018.2883726](https://doi.org/10.1109/TWC.2018.2883726).
- [47] X. Li and V. Jilkov, "Survey of maneuvering target tracking. Part I: Dynamic models," *IEEE Trans. Aerosp. Electron. Syst.*, vol. 39, no. 4, pp. 1333–1364, Oct. 2003, doi: [10.1109/TAES.2003.1261132](https://doi.org/10.1109/TAES.2003.1261132).
- [48] D. Won et al., "Weighted DOP with consideration on elevation-dependent range errors of GNSS satellites," *IEEE Trans. Instrum. Meas.*, vol. 61, no. 12, pp. 3241–3250, Dec. 2012, doi: [10.1109/TIM.2012.2205512](https://doi.org/10.1109/TIM.2012.2205512).